Resolving Early Stages of Homogeneous Iron(III) Oxyhydroxide Formation from Iron(III) Nitrate Solutions at pH 3 Using Time-Resolved SAXS

Andrew L. Rose,[*,†,‡] Mark W. Bligh,[‡,§] Richard N. Collins,[‡,§] and T. David Waite[‡,§]

[†]Southern Cross GeoScience, Southern Cross University, Lismore 2480, Australia
[‡]UNSW Water Research Centre, The University of New South Wales, Sydney 2052, Australia
[§]School of Civil and Environmental Engineering, The University of New South Wales, Sydney 2052, Australia

S *Supporting Information*

ABSTRACT: Small angle X-ray scattering (SAXS) measurements coupled to a stopped-flow device has permitted the observation of the kinetics of Fe(III) oxyhydroxide (FeOx) formation and transformation from around 1 s to 30 min after initiation under environmentally relevant conditions at pH 3. The Unified Model approach was used to determine the evolution of multiple key parameters (particle scattering mass, mean particle volume, particle concentration, particle dimensionality, and particle size) for two separate structural levels as a function of time, with the results obtained enabling clarification of the mechanisms underlying FeOx formation and transformation under these conditions. Colloidal primary particles (radius of gyration 2−10 nm) that were observable by SAXS formed within 1 s of stopping the flow and subsequently grew over several minutes, first by cluster−cluster addition and then by a monomer-addition mechanism. Aggregation of these primary particles via a secondary cluster−cluster addition mechanism simultaneously resulted in a distinct population of larger (25−40 nm radius of gyration) secondary particles. The primary particles evolved into compact spheroidal forms with fractally rough surfaces, while the secondary particles were relatively open mass fractal structures. Comparison of the observed rates of these processes with those predicted for Fe polymerization indicates that kinetics of primary particle formation were likely controlled initially by rates of exchange between water molecules coordinated with Fe and those in the bulk solution. These findings provide new insights into the mechanisms underlying FeOx formation and transformation, and the kinetics of these mechanisms, at pH 3.
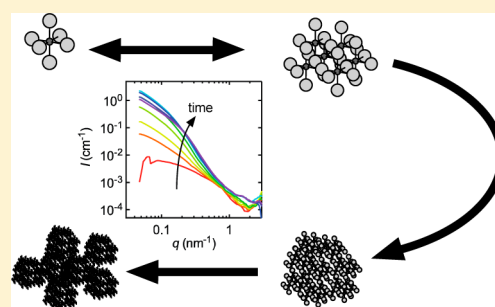
INTRODUCTION

Inorganic Fe(III) hydrolyzes to yield aquo and hydroxy complexes in aqueous solution, with complex speciation influenced by pH[1−5] and, to a lesser extent, anions such as nitrate, chloride, sulfate, and phosphate.[6,7] At sufficiently high Fe concentrations, these complexes polymerize to yield a range of Fe(III) oxyhydroxide (FeOx) species whose size and structure varies widely depending on the solution conditions.[8−10] Such reactions are likely, under certain conditions at least, to be the initial step for formation of FeOx minerals,[11,12] which are found (often abundantly) in a diverse range of environments at the Earth's surface. Small angle X-ray scattering (SAXS) is a powerful tool to investigate such processes in environmentally realistic experimental systems due to its ability to probe the size and structure of relatively small particles at sizes ranging from <1 to several hundred nanometers. The intense and highly focused X-ray radiation available at modern synchrotron light sources allows data collection in relatively dilute solutions with high temporal resolution, enabling studies at the short time scales on which the early stages of particle formation occur. Such time-resolved SAXS data have been used to determine particle formation kinetics in a range of aqueous systems[13−18] and to specifically distinguish between classical and nonclassical nucleation mechanisms.[18,19]

Models for FeOx formation and evolution from iron(III) salt solutions have previously been proposed[20−22] based on the following: (i) initial, reversible formation of small polycations consisting of monomers linked by hydroxy-bridges; (ii) further monomer addition to, and/or aggregation of, polycations to form colloidal primary particles with concomitant irreversible formation of oxo-bridges; (iii) aggregation of colloidal particles to form secondary particles; (iv) further aggregation to form settleable flocs. A major feature of this mechanism is the evolution of multiple structural levels via multiple stages of growth and aggregation. Hereafter, these structural levels will be referred to by the terminology monomers, polycations, primary particles, secondary particles, and flocs (Figure 1). In partially neutralized 100 mM Fe(NO₃)₃ solutions, Bottero et al.[23] observed linear colloidal primary particles that were
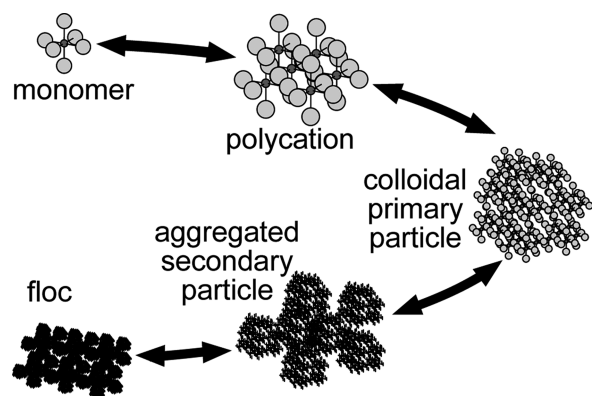
Figure 1. Conceptual model of ferric oxyhydroxide formation and transformation from $Fe(NO_3)_3$ at acidic pH, illustrating the development of multiple structural levels.

composed of three to nine polycations of radius 0.9−1.9 nm. These polycations were consistent in size with the 1.5−3.0 nm diameter spherical polycations identified by Murphy et al.[24] and Combes et al.[25] and ~4 nm diameter spherical particles found by Dousma and de Bruyn[20] under similar conditions. Development of colloidal primary particles from polycations could occur by either monomer addition or aggregation of the polycations; however, past studies have been unable to distinguish between these two pathways.[26] Furthermore, while the polycations appear to be relatively uniform spheres,[20,23−25] the size and morphology of the larger colloidal primary particles have been observed to vary with experimental conditions and aging time.[20,23−25]

While FeOx formation has previously been examined with SAXS, Fe(III) concentrations $\geq$ 0.1 M and pH < 2 were used[23,27,28] because of technical constraints. Such studies contributed valuable understanding of FeOx structure and formation processes but were unable to probe FeOx formation kinetics on short time scales under the conditions employed, with the result that details of the mechanism(s) operating at short times after initiation of reactions were unable to be completely resolved. Additionally, it is unclear whether the same processes observed in these studies operate under a wider range of conditions, for example at lower Fe concentrations or other pH values, particularly given that pH was allowed to change over the course of these earlier experiments, and the conditions employed do not typically occur widely in nature. Recent work by Jun et al.[29] and Hu et al.[19] was conducted under more environmentally relevant conditions with 100 μM Fe at a constant pH of 3.7, employing temporal resolution on the order of a few minutes over several hours. However, the first data collection did not occur until ~1 min after reagent mixing, and mixing dynamics were not well controlled, such that the very early stages of FeOx formation and transformation were unlikely to have been observed.

The aim of this study was to clarify the mechanism(s) by which FeOx formation and transformation occur in $Fe(NO_3)_3$ solutions at pH 3 at low (6 mM) ionic strength using synchrotron-based time-resolved SAXS. We sought to extend the work of Jun et al.[29] and Hu et al.[19] by the following: (i) employing rapid mixing coupled with a stopped-flow device to allow data collection within 1 s of mixing, permitting examination of earlier stages of FeOx formation under homogeneously mixed conditions; (ii) using a higher Fe concentration of 1 mM where greater scattering intensity from

particles in solution was expected, enabling observation of finer-scale features; (iii) calibrating scattering intensity on an absolute scale, enabling calculation of absolute particle number densities and volumes; (iv) using a more sophisticated modeling approach to resolve the possible simultaneous occurrence of multiple processes. At pH 3, the kinetics of FeOx polymerization are expected to be relatively slow because Fe(III) water exchange kinetics, which are thought to control the kinetics of aqueous Fe(III) polymerization,[30] are relatively slow for the dominant hydrolysis complexes in this pH range.[11] Furthermore, particles remain small enough at pH 3 to persist in suspension for many weeks,[31] which was expected to prevent substantial settling of particles during SAXS experiments.

■ EXPERIMENTAL SECTION

Small Angle X-ray Scattering. SAXS measurements were conducted on the Small and Wide Angle X-ray Scattering Beamline at the Australian Synchrotron. Experiments were conducted using a stopped flow system constructed from modular components (Figure 2). A series of independent syringe drives were used to drive three
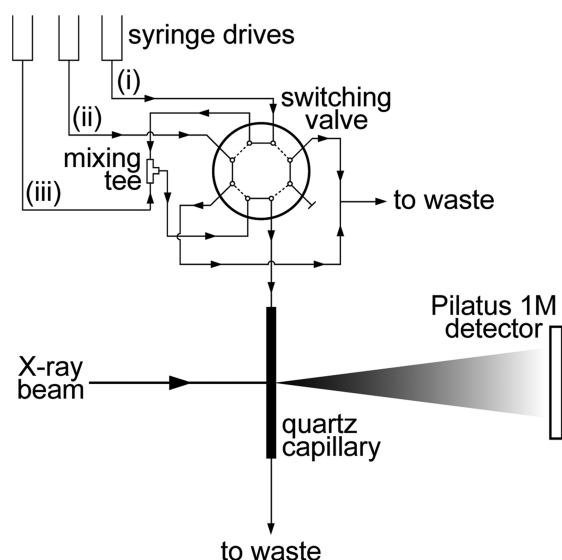

Figure 2. Configuration of apparatus for SAXS experiments with experimental solutions indicated as (i) Fe solution, (ii) HNO_3 solution, and (iii) pH buffer solution. All solutions were degassed under vacuum for 30 min prior to aspiration into the syringe drives to prevent cavitation due to pressure changes along the flow paths during experiments. The flow paths indicated by solid lines on the switching valve represent mode A while the flow paths indicated by dashed lines represent mode B. The switching valve and syringe drive units were independently and remotely controlled from outside the hutch.

solutions (working Fe(III) solution, working buffer solution, and a 10 mM HNO_3 solution) into a six-port switching valve (Valco Cheminert) and then through a static mixing tee (Upchurch), at flow rates of 400 μL s^{-1} per syringe drive (i.e., a total flow rate of 800 μL s^{-1} through the mixing tee). The mixed solution then traveled through a 2-mm diameter quartz capillary (Hampton Research) that was positioned vertically and aligned with the X-ray beam (energy 12 keV, beam size 250 μm horizontal × 150 μm vertical, flux ~2 × 10^{13} photons per second) and into a waste beaker. The high flow rate minimized the dead time between the mixer and capillary and resulted in calculated mixing times that were shorter than the expected time scale of Fe polymerization.[30] In mode A, the switching valve directed the Fe(III) solution and buffer solution through the mixing tee and then through the capillary into the waste beaker, while the HNO_3 solution ran directly to the waste beaker. In mode B, the valve directed

HNO$_3$ solution and buffer solution through the mixing tee and into the waste beaker, while the Fe(III) solution ran directly to the waste beaker. In mode B, the capillary was isolated from the flow path such that the flow inside the capillary was stopped when the valve was switched. Diverting the Fe(III) solution away from the mixing tee on activation of this mode prevented Fe(III) polymerization from occurring inside the mixing tee and also enabled rinsing of the mixing tee between runs.

Fe working solutions consisted of 2 mM Fe(NO$_3$)$_3$ in 10 mM HNO$_3$, while working buffer solutions consisted of 1.2 mM piperazine-1,4-bis(2-ethanesulfonic acid) (PIPES) at pH 3.0 amended with 1 M NaOH so that mixing of the Fe(III) working solutions with the buffer solution in a 1:1 v/v ratio resulted in the desired final pH. PIPES does not complex Fe to a measurable extent[32] and thus does not substantially affect inorganic Fe(III) concentrations or speciation, other than by pH-induced hydrolysis. The precise amount of NaOH added was determined from trial runs, in which the pH was measured when Fe(III) and buffer solutions were mixed in a manner identical to that used in the SAXS experiments, and established that pH values would remain within ±0.2 units of the target value for the duration of experiments. Final reaction mixtures contained 1 mM total Fe and 6 mM NO$_3^-$ at pH 3.0.

To commence each run, 1.5 mL of Fe solution was dispensed while the valve was in mode A to flush and fill the capillary with Fe solution. After flushing and filling were complete, 20 images were acquired every 1.05 s using an offset Pilatus 1M solid-state detector and a camera length of 3.349 m, yielding a detectable q range from 0.045 to 3.0 nm^{-1}. Subsequently, all three syringe drives were activated to each dispense 4 mL of solution at a flow rate of 400 μL s^{-1}. Midway through the pumping phase, the valve was switched from mode A to mode B to stop the flow in the capillary and rinse the flow lines. A further 1700 images were then acquired after the valve was switched. All images were radially integrated using the scatterBrain program available at the beamline to yield scattering intensity I as a function of the scattering vector q. Data were normalized to beamstop intensity and calibrated using water scattering as a standard to yield $I(q)$ on an absolute scale. For each run, the mean of the initial 20 frames was treated as representative of background scattering (due primarily to water and the capillary) and subtracted from all subsequent frames in the run. Scattering due to monomeric Fe and the pH buffer had previously been measured as negligible. Background corrected data were then smoothed on the time domain using an unweighted 5-point moving average function and a subset of data representing 100 time points that were evenly spaced on a logarithmic time scale over the experimental duration extracted for further analysis. Finally, data from each of these times were interpolated using a LOWESS smoothing function in the q domain to yield absolute scattering intensities at 100 q values that were evenly spaced on a logarithmic scale between q = 0.045 nm^{-1} and q = 3 nm^{-1}.

■ SAXS DATA ANALYSIS AND INTERPRETATION

Application of SAXS Theory to FeOx Formation and Transformation. Immediately after mixing, Fe will undergo rapid proton and ligand exchange reactions to yield monomers consisting of a central Fe atom coordinated with H$_2$O, OH$^-$, and potentially NO$_3^-$ when it is present in high concentrations. Because proton and counterion exchange occur rapidly, monomeric Fe will attain (and subsequently maintain) an equilibrium speciation prior to the onset of polymerization at constant pH and counterion concentration. This is assumed to occur instantaneously in the experimental systems investigated here.

Subsequent processes result in a hierarchy of structural levels (Figure 1) that were expected to manifest as power law regions in SAXS data collected over a sufficiently wide q range.[33] Such power law regions can, in general, be described by three associated regimes:[33,34] (i) a Porod regime characterized by a constant slope of log I vs log q, where the negative of the slope

(hereafter denoted by d) relates to the dimensionality of the structural assemblage; (ii) a Guinier regime characterized by an asymptotic value of I as q approaches zero (hereafter denoted by G); (iii) a transition regime characterized by a characteristic value of q related to R_g, the z-weighted radius of gyration of the ensemble of particles. We used Beaucage's Unified Model (UM)[33,34] to extract values of d_n, R_{gn}, and G_n for each structural level from the SAXS curves, where the subscript n indicates a particular structural level. Because of its empirical nature, the UM can be applied to any system that results in power law scattering without assumptions about the form of particles in the system. This includes particle ensembles exhibiting a wide range of forms, fractal dimensions, and dispersity, all of which influence the power law exponent but do not change the underlying power law scattering property of such systems.[35] As an alternative to the UM approach, we also attempted to fit data using the Inverse Fourier Transform method;[36] however, this approach did not yield satisfactory results for many of the SAXS curves and overall did not add useful to information to that obtained from the UM fit (see Supporting Information section 1 for further details).

Determination of d_n, R_{gn}, and G_n from the UM enables construction of the modeled scattering intensity function for structural level n, denoted by I_n, over an infinite q range. This scattering function can be used to calculate the Porod Invariant corresponding to scattering from structural level n, Q_{Pn}, where the Porod Invariant is a measure of the excess electron density of particles above the background (e.g., solvent water) within the "analytical window" of the method (i.e., within the experimentally observed q range).[37] As the excess electron density varies with the analytical window, Q_P is thus truly invariant only over a particular length scale (i.e., structural level). This approach of calculating separate Q_P functions for different structural levels has been previously used by Beaucage,[33,38] and more recently by Jacobsen et al.[39] to separately evaluate the properties of primary particles and aggregates of Mg(NH$_3$)$_6$Cl$_2$ during NH$_3$ desorption.

Values of d_n, R_{gn}, G_n, and Q_{Pn} can then be used to calculate the mean particle volume by weight, V_{Pn}, and number density of particles (number of particles per volume of solution), C_{Pn}, for particles corresponding to structural level n. Finally, relationships between these parameters over time can be used to obtain information about the mechanism(s) of particle formation and transformation.[18,19] While the possible simultaneous occurrence of multiple processes complicates analysis, at most one or two processes were hypothesized to be dominant at any given time. This approach was therefore used to unravel processes occurring at different times.

SAXS Data Analysis Methods. Values of d_n, R_{gn}, and G_n were determined using the Unified Model subject to Hammouda's modification[40] of Beaucage's original formulation,[34] which constrains the scaling factors for the Guinier (low q) and Porod (high q) terms for each power law region to ensure continuity between these terms. Parameters were obtained by nonlinear regression of the experimental $I(q)$ data using the model:

$$I(q) = \sum_{n=1}^{N} I_n(q) \tag{1}$$

where $I(q)$ represents the overall scattering of the system within the analytical window, N is the total number of structural

levels, and the scattering contribution of each structural level is given by:

$$I_n(q) = G_n e^{\left(\frac{-q^2 R_{gn}^2}{3}\right)} + G_n d_n (q R_{gn})^{-d_n}$$

$$\left(\frac{6 d_n^2}{(2 + d_n)(2 + 2 d_n)}\right)^{d_n/2} \mathrm{erf}\left(\frac{q R_{gn}}{\sqrt{6}}\right)^{3 d_n} \Gamma\left(\frac{d_n}{2}\right)$$

$$e^{\left(\frac{-q^2 R_{g(n-1)}^2}{3}\right)} \tag{2}$$

where $\mathrm{erf}(x)$ is the error function and $\Gamma(x)$ is the gamma function.

This model was applied to determine the parameters d_n, R_{gn}, and G_n using GraphPad Prism by nonlinear least-squares fitting, weighted by I^{-1} to obtain the best fit to $\log q$ vs $\log I$, and enforcing the constraints that $1 < d_n < 6$ and $R_{g(n+1)} > 2 R_{gn} > 0$ for all n. As scattering curves at $q > 1$ nm^{-1} did not display increasing intensity with decreasing q as expected for small angle scattering from a dilute solution/suspension of polydisperse particles, data for $q > 1$ nm^{-1} were excluded from the fitting procedure. Models with $N = 1$, 2, or 3 were considered initially, but $N = 1$ failed to provide good fits to the data at longer times (values of the square of the Pearson moment correlation coefficient from nonlinear regression, r^2, were substantially lower with $N = 1$ than with $N = 2$), while $N = 3$ did not result in a substantial improvement in the model fit over $N = 2$ (r^2 values from nonlinear regression were similar with $N = 2$ or 3). This does not preclude the possibility that more than two structural levels were present but implies that at most two structural levels contributed meaningfully to the observed scattering. This is addressed further in Results and Discussion. Values of fitted parameters G_1, G_2, d_1, d_2, R_{g1}, and R_{g2} were discarded if the calculated standard error of the mean (SEM) was greater than 50% of the calculated mean value itself, which indicated a poor fit of the model to the data.

The Porod Invariant, Q_{Pn}, is given by:[33]

$$Q_{Pn} = \int_0^\infty q^2 I_n \, dq = \phi_{Pn}(1 - \phi_{Pn})(\Delta \rho_n)^2 \tag{3}$$

where ϕ_{Pn} is the fraction of the sample volume occupied by particles corresponding to power law region n and $\Delta \rho_n$ is the contrast of those particles, i.e., scattering length density of the particles in excess of that due to the background solvent (water). For the primary particles, this is given by:

$$\Delta \rho_1 = \rho_{\mathrm{FeOx}} - \rho_{\mathrm{water}} \tag{4}$$

where ρ_{Feox} is the X-ray scattering length density of FeOx and ρ_{water} is the X-ray scattering length density of water. For these calculations, we used values of $\rho_{\mathrm{Feox}} = \rho_{\mathrm{ferrihydrite}} = 3.54 \times 10^{11}$ cm^{-2} and $\rho_{\mathrm{water}} = 9.5 \times 10^{10}$ cm^{-2} after Gilbert et al.[41] (with units corrected), yielding $\Delta \rho_1 = 2.59 \times 10^{11}$ cm^{-2}.

Values of Q_{P1} and Q_{P2} were determined at each of the 100 time points used in the previously described data analyses by numerically integrating calculated values of $q^2 I_n$ over the q range of 0−2 nm^{-1} using GraphPad Prism, where I_n was calculated from eq 2 using determined values of G_1, G_2, d_1, d_2, R_{g1}, and R_{g2}. Additionally, the "overall" empirical Porod Invariant, Q_P^* was determined by numerical integration of $q^2 I^*$ over the experimentally measured q range up to 2 nm^{-1}, where I^* represents the experimentally measured absolute scattering intensity.

Values of V_{Pn} and C_{Pn} were calculated using the relationships:[18]

$$V_{Pn} = \frac{2\pi^2 G_n}{Q_{Pn}} \tag{5}$$

$$C_{Pn} = \frac{(Q_{Pn})^2}{4\pi^4 (\Delta \rho)^2 G_n} \tag{6}$$

RESULTS AND DISCUSSION

Scattering Intensity. Porod plots of $\log I$ vs $\log q$ (Figure 3A) were relatively featureless but exhibited at least one power
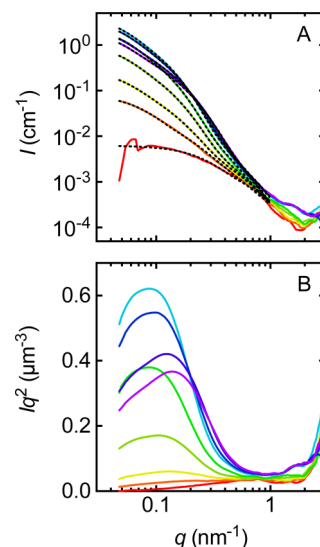
Figure 3. (A) Porod plots and (B) Kratky plots as a function of time. Solid lines represent the mean from duplicate experiments. Colors indicate times after mixing (red = 10 s, orange = 20 s, yellow = 30 s, lime green = 60 s, green = 120 s, pale blue = 300 s, dark blue = 600 s, dark purple = 1200 s, and violet = 1750 s after mixing). Error bars, which were negligibly small in most cases, are omitted for clarity. Dashed lines in panel A represent the fit of the UM to each scattering curve.

law regime (over a limited q range) as indicated by a constant slope. These plots suggest that the high q region may contain diffraction peaks indicative of ordered domains within the FeOx particles; however, these data were not interpreted further, as the limited q range and low scattering intensity in this region meant that any information obtained was not considered reliable. At low q, a flat Guinier region (which should theoretically occur as $q \to 0$) was only present at relatively short times after stopping the flow. Scattering intensity increased over time throughout the measured q range up to $t = 300$ s but began to decrease at lower q values after $t = 600$ s (Figure 3). Fouling of the capillary was also visible after experimental runs, implying that precipitation and/or adsorption of FeOx occurred at the capillary surface to some extent. Pontoni et al.[42] observed a decrease in overall scattering intensity during SAXS experiments of calcium carbonate precipitation and ascribed this decrease to particle dissolution, sedimentation, and/or adsorption on the capillary walls. The decrease in scattering intensity in the experiments described here only occurred at low q values in our experiments, in contrast to the observations of Pontoni et al.,[42] implying that if

this was related to the fouling of the capillary, larger particles were being preferentially adsorbed. Dynamic light scattering (DLS) measurements exhibited no change in count rate over 30 min (see Supporting Information section 2), implying that sedimentation was unlikely to have occurred. Additional useful information on particle sizes and size distributions could not be reliably obtained from DLS because of the confounding influence of polydispersity and because information about primary particles within aggregated structures cannot be resolved by this technique. The potential effects of surface precipitation and/or adsorption of larger particles to the capillary are considered further later.

Kratky plots of Iq^2 vs log q (Figure 3B) exhibited a single distinct peak in the SAXS region ($0 < q < 1$ nm^{-1}), which is typically indicative of globular type structures. Such curves are also integrable over this q range, supporting valid calculation of Q_P.

Particle Dimensionality and Size. Good fits of the UM to scattering curves were difficult to obtain at $t < 10$ s because of weak scattering intensity. Good fits were obtained at longer times (Figure 3A) for the region of $q < 1$ nm^{-1}, permitting determination of d, R_g, and G for each power law region as a function of time after stopping the flow (Figure 4; values of G
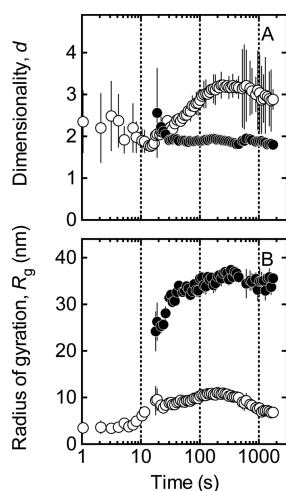

Figure 4. Evolution of (A) dimensionality, d, and (B) radius of gyration, R_g, calculated using the UM as a function of time. Open circles represent parameter values (d_1 and R_{g1}) for particles responsible for scattering in the high q power law region and closed circles represent parameter values (d_2 and R_{g2}) for particles responsible for scattering in the low q power law region. Symbols represent the mean and error bars the standard error of the mean from nonlinear regression fitting of the UM to the experimental scattering data.

are not shown). The dimensionality parameter d_1 increased from ~2 just after stopping the flow to ~3 after $t = 100$ s and remained similar for the remainder of the experimental duration (Figure 4A). In a low dispersity (monodisperse) ensemble of particles, values of d_1 around 2 during the initial ~30 s would imply a plateletlike or mass fractal particle morphology, while values of d_1 between 3 and 4 at later stages of the experiment would imply a surface fractal object.[35] However, high dispersity can result in a power law exponent less than the true fractal dimension of the object(s) such that a polydisperse ensemble of nonfractal scatterers could also yield the observed values of d_1.[35,43] Additional evidence from transmission electron microscopy (TEM) was therefore used

to constrain these possibilities. Although we did not perform sufficient TEM measurements to form a statistically rigorous conclusion, individual primary particles in TEM images obtained on samples that were snap frozen at $t = 10$ s and $t = 1000$ s appeared relatively nonporous and spheroidal in shape even as early as $t = 10$ s (Figure S1 in Supporting Information). A relatively monodisperse population of spheroidal particles should result in distinctive undulations in the Porod plot at high q, which were not observed. The calculated values of d_1 may thus reflect scattering from a polydisperse ensemble of compact spheroidal particles with either a smooth or rough (fractal) surface, with changes in d_1 over time likely due, at least in part, to changes in the degree of dispersity.

In contrast, d_2 maintained relatively constant values of around 1.9 from $t = 30$ s (when this structural level became discernible from scattering curves) until the conclusion of experimental runs. While this could again result from a highly disperse ensemble of nonfractal or surface fractal particles, noninteger values of $d < 2$ typically result from mass fractal structures. Formation of aggregates possessing mass fractal structures is observed during cluster−cluster modes of particle aggregation, with a fractal dimension $D_f = 1.80$ (where $D_f = d$ for a mass fractal) typical for a cluster−cluster diffusion-limited aggregation (DLA) process and $D_f = 2.09$ typical for reaction limited aggregation (RLA).[44] Because of possible effects of dispersity, it is again impossible to determine the mode of aggregation from the SAXS data alone with certainty, but because polydispersity tends to decrease values of d, and $d_2 > 1.80$, DLA would appear unlikely. TEM images of larger aggregate structures at $t = 1000$ s (Figure S1, Supporting Information) also appear more consistent with relatively compact mass fractal structures typified by RLA than more open structures typified by DLA.[44,45] RLA would be expected for FeOx in 6 mM NO$_3^-$ at pH 3.0 because it is most likely when a substantial repulsive charge barrier exists between primary particles.[31] However, such a conclusion is tentative, as the freeze-drying processes employed during sample preparation for TEM could conceivably result in compaction of loose structures, despite use of a protocol to minimize this (see Supporting Information). In agreement with the SAXS data, such aggregate structures were not observed in TEM images from samples taken at $t = 10$ s.

R_{g1} increased from ~3 nm at $t = 1$ s to ~9 nm at $t = 20$ s and then remained relatively constant between 7 and 10 nm for the rest of the experimental duration. R_{g2} increased relatively rapidly from ~25 nm at $t = 20$ s to ~35 nm from $t = 60$ s until the conclusion of experimental runs. At the order of magnitude level, values of R_{g1} appeared consistent with the typical size of relatively well-defined particles observed by TEM at both $t = 10$ s and $t = 1000$ s, while values of R_{g2} appeared broadly consistent with the size of the larger aggregate structures observed at $t = 1000$ s by TEM, although such structures were not very sharply defined (Figure S1, Supporting Information).

The ability to characterize a particular structural level is limited by the analytical window. As the maximum value of $q = 3.0$ nm^{-1} in this work corresponds to length scales of ~2 nm, it was expected that power law scattering associated with highest values of q in this work would correspond to the structural level of colloidal primary particles (Figure 1); smaller polycations of up to several nanometers in diameter, as determined in other studies,[23−25] would scatter too weakly to be detected under the experimental conditions used. The colloidal primary particles in this work may thus be either a distinct structural level formed

by aggregation of these polycations, or polycations that have grown sufficiently large to be detectable through monomer addition.

Particle Volumes and Concentration. The calculated sum of Q_{P1} and Q_{P2} reconciled well with values of Q_P^* at all times, indicating that the modeled components accurately captured the total scattering mass of the system (Figure 5) and
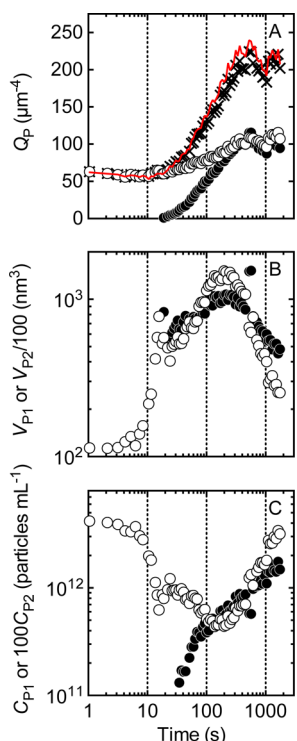

Figure 5. Evolution of (A) the Porod invariant, Q_P, (B) mean volume by weight of each particle, V_P, and (C) particle concentration, C_P, as a function of time. Open circles represent parameter values for particles responsible for scattering in the high q power law region, closed circles represent parameter values for particles responsible for scattering in the low q power law region, and crosses represent the sum of the two. The solid red line in panel A represents the overall invariant function Q_P^* calculated by integration of Kratky plots of experimental I vs q data. Seven data points in the interval $10 < t < 20$ s where $10^7 < C_{P2} < 10^9$ particles mL^{-1} are omitted from panel C to enable clear presentation of trends in the remaining data.

thereby supporting application of the UM with two structural levels. Q_{P1} was relatively constant at ~60 μm^{-4} from 1 to 20 s after stopping the flow and then increased monotonically to ~100 μm^{-4} until $t = 300$ s, before remaining relatively constant again until the conclusion of the experimental runs. The relatively high value of Q_{P1} 1 s after stopping the flow compared with its value at the conclusion of the experiment indicates that about 50% of the total scattering mass of the primary particles had already formed within 1 s. In contrast, Q_{P2} increased over time from <1 μm^{-4} at 20 s after stopping the flow (when calculation of Q_{P2} became feasible) to ~100 μm^{-4} at 300 s, implying aggregation of the primary particles during this period. After 300 s, Q_{P2} remained relatively constant until the conclusion of the experimental runs. During this latter period, Q_{P1} and Q_{P2} both contributed approximately equally to the total scattering power of the system.

Assuming that FeOx primary particles have a similar density to ferrihydrite, it is possible to compare measured values of Q_{P1}

with theoretical calculations. Using a value for the Fe-normalized molar volume of FeOx = 4×10^{-29} m^3.(atom Fe)$^{-1} \times 6.022 \times 10^{23}$ atom Fe (mol Fe)$^{-1} = 2.4 \times 10^{-5}$ m^3 mol^{-1},[46] when all Fe is present as primary particles, we obtain $\phi_{P1} = 10^{-3}$ mol Fe L$^{-1} \times 10^3$ L m$^{-3} \times 2.4 \times 10^{-5}$ m^3 mol$^{-1} = 2.4 \times 10^{-5}$. Hence from eq 3, when all Fe is present as primary particles, $Q_{P1} = 2.4 \times 10^{-5} \times (2.59 \times 10^{11}$ cm$^{-2})^2 \times 10^{-16}$ cm^4 μm$^{-4} = 162$ μm^{-4}. The maximum value of 116 μm^{-4} for Q_{P1} calculated from the UM fit parameters is 28% less than the theoretical value, with the discrepancy likely due to a combination of uncertainty in the molar volume of FeOx and adsorption of FeOx to the capillary walls during the latter stages of the experiment. This is discussed further below.

C_{P1} was 4.3×10^{12} particles mL^{-1} within 1 s of stopping the flow and then gradually decreased to $\sim4 \times 10^{11}$ particles mL^{-1} at $t = 300$ s (Figure 5B). The fact that C_{P1} was greatest at 1 s after stopping the flow implies that nucleation of the primary particles was essentially complete within 1 s. V_{P1} increased monotonically from $\sim10^2$ nm^3 at 1 s after stopping the flow to a maximum value of $\sim1.5 \times 10^3$ nm^3 at $t = 300$ s. In contrast, C_{P2} increased steadily from $<10^9$ particles mL^{-1} 30 s after stopping the flow (when this structural level was first detected) to $\sim7 \times 10^9$ particles mL^{-1} at $t = 300$ s. The mean volume of these secondary particles was a factor of ~100 greater than that of V_{P1} at all times and followed an almost identical trend to the mean volume of the primary particles, with V_{P2} also increasing to a maximum value at 300 s.

At times >300 s, calculated values of C_{P1} and C_{P2} continued to increase, accompanied by decreases in V_{P1}, V_{P2}, R_{g1}, and R_{g2} and a plateau in values of Q_{P1}, Q_{P2}, and Q_P^*. The difference between the theoretical value and the maximum calculated value of Q_{P1} from the UM fit parameters suggests that the amount of FeOx adsorbed to the capillary may have been sufficient to decrease the total scattering mass (adsorbed and in solution or suspension) within the X-ray beam path by up to 28%. The loss of a very small mass of large particles can have a large and disproportionate effect on scattering intensity at low q, resulting in an apparent (artificial) increase in values of C_{P1} and C_{P2} and apparent (artificial) decrease in values of V_{P1} and V_{P2} from the UM fit to simulate the decrease in scattering intensity at low q. Adsorption of large particles to the capillary wall thus appears to be the most likely explanation for the decrease in mean particle volumes and sizes at $t > 300$ s, consistent with visual observations of capillary fouling and with similar observations described by Liu et al.[18] during investigations of CaCO$_3$ formation. Consequently, calculated values of C_{P1}, C_{P2}, V_{P1}, and V_{P2} must be considered unreliable at $t > 300$ s, and no further attempt is made to interpret particle formation mechanisms in this time period. While this appears the simplest and most obvious explanation for these observations, however, it does not preclude the possibility of other physicochemical processes from contributing (for example, similar behavior was observed by Bottero et al.[23] over time scales comparable to those in this work, although at different pH and total Fe concentrations).

Mechanism of Particle Formation and Growth. Fe polymerization kinetics are thought to be largely controlled by water loss rates from the Fe hydrolysis species present at various pH values, with much faster rates for more hydrolyzed species (167 s^{-1} for [Fe(OH$_2$)$_6$]$^{3+}$, 4.5×10^5 s^{-1} for [Fe(OH$_2$)$_5$(OH)]$^{2+}$, 1.0×10^6 s^{-1} for [Fe(OH$_2$)$_4$(OH)$_2$]$^+$, and 6.3×10^7 s^{-1} for [Fe(OH$_2$)$_3$(OH)$_3$]^0 (aq)).[30] The data presented here imply that the initial polymerization process

(nucleation) is largely complete within 1 s. This is consistent with a predicted reaction half-time of 0.7 s at pH 3 with 1 mM total Fe if polymerization kinetics are governed by reactions between all monomeric hydrolysis species,[30] but much less than a predicted half-time of ~70 s if Fe polymerization kinetics are governed by reactions of $[Fe(OH_2)_3(OH)_3]^0$ only, with the longer half-time in the latter case because the concentration of $[Fe(OH_2)_3(OH)_3]^0$ is exceedingly low at pH 3, despite its rapid water loss kinetics. The measured time for nucleation here is also 1−2 orders of magnitude less than previously measured half-times under conditions where $[Fe(OH_2)_3(OH)_3]^0$ was thought to control nucleation kinetics.[47] Thus, the data presented here suggest that the formation of polycations most likely results from polymerization reactions between multiple different monomeric Fe hydrolysis species.

The combination of increasing V_{P1} and decreasing C_{P1} indicates growth of larger primary particles at the expense of smaller particles from 1 to 300 s. This could result either from a dissolution−reprecipitation process (i.e., Ostwald Ripening)[19] or from cluster−cluster addition to yield particles with similar structural properties to the original particles (for example by particle coalescence, such that formation of the larger particles did not constitute a new structural level). During the period 1− 20 s, Q_{P1} remained relatively constant but then from 20 to 300 s increased substantially, indicating the occurrence of particle growth from 20 to 300 s by addition of Fe monomers or polycations smaller than the detection window to existing FeOx particles. Consistent with this process, d_1 increased from around 2 to 3 from 1 to 300 s, implying a possible change in the primary particles from more open structures (e.g., sheetlike objects or mass fractals) into compact objects with a rough surface and/or, most likely, decreasing polydispersity. The combination of increasing V_{P2} and C_{P2} from the appearance of secondary particles at 20 s until ~300 s indicates formation and, potentially, simultaneous growth of particles during this period, with a mass fractal structure implied by values of d_2 around 1.9.

The relationship between V_P and R_g provides additional information on the shape and growth mechanism of particles.[18,48] Plots of log R_g against log V_P exhibit a slope that is characteristic of particle dimensionality, such that a spherical object will yield a slope of 1/3, a rodlike object a slope of 1, and sheets, Gaussian coils, or fractal structures a slope somewhere between.[48] As shown in Figure 6A and Table 1, a plot of log R_{g1} against log V_{P1} yielded a slope of ~0.9 during the initial few seconds, implying a relatively low particle dimensionality. After 10 s, the slope decreased substantially to a value slightly less than 1/3, confirming the evolution of the primary particles to a (near) spheroidal shape by around $t = 10$ s. The trend for $t > 10$ s is consistent with the trend in d_1; however, the trend for $t < 10$ s implies a particle dimensionality of ~1.1, compared to the value of d_1 of ~2 obtained from the UM fit (Figure 4). The precise reasons for this discrepancy are unclear but may be at least in part due to relatively large errors in values of both d_1 and R_{g1} at these early times. In contrast, the slope of a plot of log R_{g2} against log V_{P2} yielded a value of ~0.4 from 10 to 300 s, consistent with the modeled value of d_2 during this period. Overall, this analysis was consistent with the UM fitting procedure, providing further confidence in the results obtained.

While the slope of log R_g against log V_P depends only on particle dimensionality, comparison with the slope of plots of log R_g against log G enable discrimination between a monomer addition mechanism and a Smoluchowski-type cluster−cluster
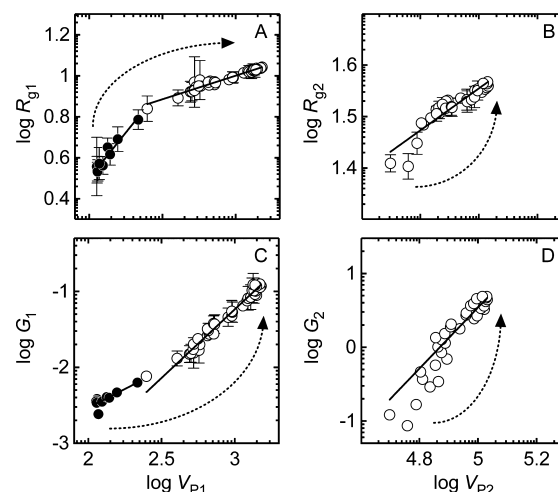

Figure 6. Logarithmic relationships between R_g, G, and V_P for (A and C) primary particles and (B and D) secondary particles. Symbols represent the mean and error bars the standard error of the mean from nonlinear regression fitting of the UM to the experimental scattering data. Filled symbols indicate data for $t \leq 10$ s, and open symbols represent data for $10 < t < 300$ s. Solid lines represent linear regression of the data for each of the time intervals, and the dotted arrows indicate the direction of evolution of the system with increasing time. Data are not presented for the time interval of 300−1800 s because of the confounding influence of likely particle adsorption to the capillary wall.

Table 1. Slopes from Linear Regression of log R_g against log V_P and log G against log V_P for the Each Structural Level during Time Intervals of 1−10 s and 10−300 s

parameter 1	parameter 2	slope over indicated time interval[a]	
		1−10 s	10−300 s
log R_{g1}	log V_{P1}	0.895 ± 0.077 (0.929)	0.230 ± 0.009 (0.948)
log R_{g2}	log V_{P2}	ND[b]	0.408 ± 0.108 (0.870)
log G_1	log V_{P1}	0.980 ± 0.135 (0.836)	1.81 ± 0.09 (0.963)
log G_2	log V_{P2}	ND[b]	ND[c]

[a]Values are reported as best fit ± standard error, with the r^2 value for the regression shown in parentheses. Data are not reported for the time interval of 300−1800 s because of the confounding influence of likely particle adsorption to the capillary wall. [b]Not determined, as no data were available during this period. [c]Not reported, as the slope from linear regression was statistically ambiguous.

addition mechanism.[18,48] More specifically, the slope of log R_g against log G should be the same as that for log R_g against log V_P in the case of a cluster−cluster addition mechanism but only half that for log R_g against log V_P in the case of a monomer addition mechanism. Plotting log G against log V_P (therefore eliminating R_g from the relationships) enables direct comparison, with a corresponding slope of 2 expected for a monomer addition mechanism and 1 for a cluster−cluster addition mechanism. This relationship is also valid for a polydisperse distribution of particle sizes, provided the nature of the distribution does not change with increasing particle size and volume.[18]

The relationship between log G_1 and log V_{P1} (Figure 6 and Table 1) implies that primary particle formation was controlled predominantly by cluster−cluster addition from 1 to 10 s after mixing and then followed by monomer addition from 10 to 300 s. These conclusions must be interpreted with some caution, particularly in the transition period between the two

mechanisms, as it seems likely that the dispersity of the particle population also decreased during this period. In this context, monomer addition could involve addition of any particles smaller than the analytical window to existing primary particles, not necessarily just addition of Fe monomers in the strict sense. Thus, the evidence for such a mechanism does not eliminate the possibility that primary particles form through aggregation of polycations too small to be observed by SAXS in this work. Cluster–cluster addition is expected to yield values of d_1 around 2, while a monomer addition growth mechanism is expected to result in values of d_1 of ~3 for reaction-limited kinetics (e.g., polymerization kinetics limited by water loss rates),[44] again implying consistency with results from the UM fit. Furthermore, the fact that these primary particles are not smooth colloids strongly argues for kinetic rather than equilibrium control of their formation.[44] From 300 to 1800 s, it is not possible to draw conclusions about the likely mechanisms for particle formation given that the size and volume of secondary particles were decreasing during this period, most likely because of adsorption of large particles to the capillary wall as discussed previously. Additionally, the slope from linear regression of log G_2 against log V_{P2} from 10 to 300 s was statistically ambiguous, such that no reliable information on the mechanism of secondary particle formation could be derived from this analysis. However, values for d_2 of around 1.9 are most consistent with particle–particle addition,[44] suggesting the likelihood that the secondary particles form from aggregation of primary particles in such a way that the structure of the primary particles is preserved within mass fractal aggregate structures.

CONCLUSIONS

Coupling of SAXS with a stopped-flow device has permitted the observation of the kinetics of FeOx formation and transformation from 1 s to 30 min after initiating Fe polymerization at pH 3. The mechanism of FeOx formation from 1 mM $Fe(NO_3)_3$ at pH 3 can be described by the following steps:

1. Rapid (<1 s) polymerization reactions between multiple monomeric Fe hydrolysis species, which are likely controlled by water exchange kinetics, to yield small polycations;
2. Formation of low dimensionality and/or polydisperse primary particles from 1 to 10 s after formation that evolve through a predominantly cluster–cluster addition mechanism to yield larger primary particles without a substantial change in overall particle structure;
3. Ongoing growth of primary particles through a monomer addition mechanism (where the "monomer" may either be truly monomeric Fe, or polycations <2 nm that were too small to be detected by SAXS in the present experiment) from 10 to 300 s to yield colloidal primary particles with radii of 3–10 nm, with simultaneous evolution to spheroidal shapes with fractally rough surfaces;
4. Aggregation (most likely reaction-limited) of colloidal primary particles through a cluster–cluster addition mechanism from 20 to 300 s to yield secondary particles with radii of gyration from 25 to 40 nm and mass fractal structures.

After 300 s, decreasing average particle volumes for both the primary and secondary particles were observed. This appears most likely due to adsorption of larger particles to the capillary

wall; however, a definitive explanation for this observation is not possible without additional experimental evidence.

The findings of this work are generally consistent with previously developed general models for FeOx formation and transformation under similar conditions. They furthermore support the notion that the initial polymerization process is likely to be governed by water exchange kinetics from the monomeric species present. While the kinetics and mechanisms of particle growth were successfully observed by SAXS, initial development of the smallest observable particles occurred too quickly to be observed under the conditions employed. Due to limitations inherent with SAXS (e.g., detection limits for Fe and temporal resolution), investigation of the very first steps under conditions typical of natural systems will thus require the use of additional techniques. However, the insight gained in this study will be invaluable for interpretation of such studies and provides further understanding of the mechanisms of FeOx formation and transformation that are likely to prevail under a range of natural conditions.

■ ASSOCIATED CONTENT

Ⓢ Supporting Information

Discussion of the Inverse Fourier Transform method for fitting SAXS data, and methods and results from complementary dynamic light scattering and transmission electron microscopy studies. This material is available free of charge via the Internet at http://pubs.acs.org.

■ AUTHOR INFORMATION

Corresponding Author

*Tel: +61 2 6620 3189. Fax: +61 2 6626 9499. E-mail: andrew.rose@scu.edu.au.

Notes

The authors declare no competing financial interest.

■ ACKNOWLEDGMENTS

■ REFERENCES

(1) Byrne, R. H.; Luo, Y. R.; Young, R. W. Iron hydrolysis and solubility revisited: Observations and comments on iron hydrolysis characterizations. *Mar. Chem.* **2000**, *70* (1–3), 23–35.

(2) Perera, W. N.; Hefter, G. Mononuclear cyano- and hydroxo-complexes of iron(III). *Inorg. Chem.* **2003**, *42* (19), 5917–5923.

(3) Stefánsson, A. Iron(III) hydrolysis and solubility at 25°C. *Environ. Sci. Technol.* **2007**, *41* (17), 6117–6123.

(4) Baes, C. F. J.; Mesmer, R. E. *The Hydrolysis of Cations*; John Wiley & Sons: New York, 1976.

(5) Millero, F. J.; Woosley, R. The hydrolysis of Al(III) in NaCl solutions - A model for Fe(III). *Environ. Sci. Technol.* **2009**, *43* (6), 1818–1823.

(6) Byrne, R. H.; Yao, W.; Luo, Y.-R.; Wang, B. The dependence of Fe^III hydrolysis on ionic strength in NaCl solutions. *Mar. Chem.* **2005**, *97* (1–2), 34–48.

(7) Millero, F. J.; Yao, W.; Aicher, J. The speciation of Fe(II) and Fe(III) in natural waters. *Mar. Chem.* **1995**, *50* (1–4), 21–39.

(8) Murphy, P. J.; Posner, A. M.; Quirk, J. P. Characterization of hydrolyzed ferric ion solutions a comparison of the effects of various anions on the solutions. *J. Colloid Interface Sci.* **1976**, *56* (2), 312–319.

(9) Dousma, J.; Van den Hoven, T. J.; De Bruyn, P. L. The influence of chloride ions on the formation of iron(III) oxyhydroxide. *J. Inorg. Nuclear Chem.* **1978**, *40* (6), 1089–1093.

(10) Dousma, J.; den Ottelander, D.; de Bruyn, P. L. The influence of sulfate ions on the formation of iron(III) oxides. *J. Inorg. Nuclear Chem.* **1979**, *41* (11), 1565–1568.

(11) Blesa, M. A.; Matijević, E. Phase transformations of iron oxides, oxohydroxides, and hydrous oxides in aqueous media. *Adv. Colloid Interface Sci.* **1989**, *29* (3–4), 173–221.

(12) Flynn, C. M., Jr. Hydrolysis of inorganic iron(III) salts. *Chem. Rev.* **1984**, *84* (1), 31–41.

(13) Tobler, D. J.; Shaw, S.; Benning, L. G. Quantification of initial steps of nucleation and growth of silica nanoparticles: An in-situ SAXS and DLS study. *Geochim. Cosmochim. Acta* **2009**, *73* (18), 5377–5393.

(14) Fan, W.; Ogura, M.; Sankar, G.; Okubo, T. In situ small-angle and wide-angle X-ray scattering investigation on nucleation and crystal growth of nanosized zeolite A. *Chem. Mater.* **2007**, *19* (8), 1906–1917.

(15) Harada, M.; Katagiri, E. Mechanism of silver particle formation during photoreduction using in situ time-resolved SAXS analysis. *Langmuir* **2010**, *26* (23), 17896–17905.

(16) Bolze, J.; Peng, B.; Dingenouts, N.; Panine, P.; Narayanan, T.; Ballauff, M. Formation and growth of amorphous colloidal CaCO_3 precursor particles as detected by time-resolved SAXS. *Langmuir* **2002**, *18* (22), 8364–8369.

(17) Marmiroli, B.; Grenci, G.; Cacho-Nerin, F.; Sartori, B.; Ferrari, E.; Laggner, P.; Businaro, L.; Amenitsch, H. Free jet micromixer to study fast chemical reactions by small angle X-ray scattering. *Lab Chip* **2009**, *9* (14), 2063–2069.

(18) Liu, J.; Pancera, S.; Boyko, V.; Shukla, A.; Narayanan, T.; Huber, K. Evaluation of the particle growth of amorphous calcium carbonate in water by means of the Porod invariant from SAXS. *Langmuir* **2010**, *26* (22), 17405–17412.

(19) Hu, Y.; Lee, B.; Bell, C.; Jun, Y.-S. Environmentally abundant anions influence the nucleation, growth, ostwald ripening, and aggregation of hydrous Fe(III) oxides. *Langmuir* **2012**, *28* (20), 7737–7746.

(20) Dousma, J.; de Bruyn, P. L. Hydrolysis-precipitation studies of iron solutions. II. Aging studies and the model for precipitation from Fe(III) nitrate solutions. *J. Colloid Interface Sci.* **1978**, *64* (1), 154–170.

(21) Dousma, J.; De Bruyn, P. L. Hydrolysis-precipitation studies of iron solutions. I. Model for hydrolysis and precipitation from Fe(III) nitrate solutions. *J. Colloid Interface Sci.* **1976**, *56* (3), 527–539.

(22) Schneider, W. Hydrolysis of iron(III) - chaotic olation versus nucleation. *Comments Inorg. Chem.* **1984**, *3* (4), 205–223.

(23) Bottero, J. Y.; Tchoubar, D.; Arnaud, M.; Quienne, P. Partial hydrolysis of ferric nitrate salt. Structural investigation by dynamic light scattering and small-angle X-ray scattering. *Langmuir* **1991**, *7* (7), 1365–1369.

(24) Murphy, P. J.; Posner, A. M.; Quirk, J. P. Characterization of partially neutralized ferric nitrate solutions. *J. Colloid Interface Sci.* **1976**, *56* (2), 270–283.

(25) Combes, J. M.; Manceau, A.; Calas, G.; Bottero, J. Y. Formation of ferric oxides from aqueous solutions: A polyhedral approach by X-ray absorption spectroscopy: I. Hydrolysis and formation of ferric gels. *Geochim. Cosmochim. Acta* **1989**, *53* (3), 583–594.

(26) Rose, J.; Manceau, A.; Masion, A.; Bottero, J. Y. Structure and mechanisms of formation of FeOOH(NO_3) oligomers in the early stages of hydrolysis. *Langmuir* **1997**, *13* (12), 3240–3246.

(27) Masion, A.; Rose, J.; Bottero, J.-Y.; Tchoubar, D.; Elmerich, P. Nucleation and growth mechanisms of iron oxyhydroxides in the presence of PO_4 ions. 3. Speciation of Fe by small angle X-ray scattering. *Langmuir* **1997**, *13* (14), 3882–3885.

(28) Tchoubar, D.; Bottero, J. Y.; Quienne, P.; Arnaud, M. Partial hydrolysis of ferric chloride salt. Structural investigation by photon-correlation spectroscopy and small-angle X-ray scattering. *Langmuir* **1991**, *7* (2), 398–402.

(29) Jun, Y.-S.; Lee, B.; Waychunas, G. A. In situ observations of nanoparticle early development kinetics at mineral−water interfaces. *Environ. Sci. Technol.* **2010**, *44* (21), 8182–8189.

(30) Pham, A. N.; Rose, A. L.; Feitz, A. J.; Waite, T. D. Kinetics of Fe(III) precipitation in aqueous solutions at pH 6.0−9.5 and 25°C. *Geochim. Cosmochim. Acta* **2006**, *70* (3), 640–650.

(31) Gilbert, B.; Lu, G.; Kim, C. S. Stable cluster formation in aqueous suspensions of iron oxyhydroxide nanoparticles. *J. Colloid Interface Sci.* **2007**, *313* (1), 152–159.

(32) Kandegedara, A.; Rorabacher, D. B. Noncomplexing tertiary amines as "better" buffers covering the range of pH 3−11. Temperature dependence of their acid dissociation constants. *Anal. Chem.* **1999**, *71* (15), 3140–3144.

(33) Beaucage, G. Small-angle scattering from polymeric mass fractals of arbitrary mass-fractal dimension. *J. Appl. Crystallogr.* **1996**, *29* (2), 134–146.

(34) Beaucage, G. Approximations leading to a unified exponential/power-law approach to small-angle scattering. *J. Appl. Crystallogr.* **1995**, *28* (6), 717–728.

(35) Schmidt, P. W. Small-angle scattering studies of disordered, porous and fractal systems. *J. Appl. Crystallogr.* **1991**, *24* (5), 414–435.

(36) Glatter, O. Determination of particle-size distribution functions from small-angle scattering data by means of the indirect transformation method. *J. Appl. Crystallogr.* **1980**, *13* (1), 7–11.

(37) Spalla, O. General theorems in small-angle scattering. In *Neutron, X-rays and Light. Scattering Methods Applied to Soft Condensed Matter*; Zemb, T.; Lindner, P., Eds.; Elsevier: Amsterdam, 2002; pp 49−71.

(38) Beaucage, G.; Kammler, H. K.; Pratsinis, S. E. Particle size distributions from small-angle scattering using global scattering functions. *J. Appl. Crystallogr.* **2004**, *37* (4), 523–535.

(39) Jacobsen, H. S.; Hansen, H. A.; Andreasen, J. W.; Shi, Q.; Andreasen, A.; Feidenhans'l, R.; Nielsen, M. M.; Ståhl, K.; Vegge, T. Nanoscale structural characterization of Mg(NH_3)_6Cl_2 during NH_3 desorption: An in situ small angle X-ray scattering study. *Chem. Phys. Lett.* **2007**, *441* (4−6), 255–260.

(40) Hammouda, B. Analysis of the Beaucage model. *J. Appl. Crystallogr.* **2010**, *43* (6), 1474–1478.

(41) Gilbert, B.; Ono, R. K.; Ching, K. A.; Kim, C. S. The effects of nanoparticle aggregation processes on aggregate structure and metal uptake. *J. Colloid Interface Sci.* **2009**, *339* (2), 285–295.

(42) Pontoni, D.; Bolze, J.; Dingenouts, N.; Narayanan, T.; Ballauff, M. Crystallization of calcium carbonate observed in-situ by combined small- and wide-angle X-ray scattering. *J. Phys. Chem. B* **2003**, *107* (22), 5123–5125.

(43) Schmidt, P. Interpretation of small-angle scattering curves proportional to a negative power of the scattering vector. *J. Appl. Crystallogr.* **1982**, *15* (5), 567–569.

(44) Schaefer, D. W. Polymers, fractals, and ceramic materials. *Science* **1989**, *243* (4894), 1023–1027.

(45) Meakin, P. Aggregation kinetics. *Phys. Scr.* **1992**, *46* (4), 295.

(46) Marchand, P.; Rancourt, D. G. General model for the aqueous precipitation of rough-surface nanocrystals and application to ferrihydrite genesis. *Am. Mineral.* **2009**, *94* (10), 1428–1439.

(47) Grundl, T.; Delwiche, J. Kinetics of ferric oxyhydroxide precipitation. *J. Contam. Hydrol.* **1993**, *14* (1), 71–87.

(48) Liu, J.; Rieger, J.; Huber, K. Analysis of the nucleation and growth of amorphous CaCO_3 by means of time-resolved static light scattering. *Langmuir* **2008**, *24* (15), 8262–8271.